Chemical Engineering Research and Design 217 (2025) 399–415

Contents lists available at ScienceDirect

Chemical Engineering Research and Design

journal homepage: www.elsevier.com/locate/cherd

Numerical hydrodynamic characterization for the design of a lab-scale jet-loop reactor

Ronny Gueguen [a,b], Hervé Neau [a], William Benguigui [c,d], Anne-Marie Billet [b], Carine Julcour [b], Renaud Ansart [b,*]

[a] Institut de Mécanique des Fluides (IMFT), Université de Toulouse, CNRS, INPT, UPS, Toulouse, France
[b] Laboratoire de génie Chimique (LGC), Université de Toulouse, CNRS, INPT, UPS, Toulouse, France
[c] Fluid Mechanics, Energy and Environment Department, EDF R&D, Chatou, France
[d] IMSIA, UMR EDF/CNRS/CEA/ENSTA 9219, Université Paris-Saclay, Palaiseau, France

ARTICLE INFO

Keywords:
Computational fluid dynamics
Chemical reactor design
Jet-loop reactor
Hydrodynamic 0D model
Residence time distribution
Immersed boundary

ABSTRACT

The jet-loop reactor is a powerful tool for analyzing the kinetics of heterogeneous catalytic reactions due to its high mixing degree. Indeed, the high momentum gas flow injected within the loop induces a large gas recycling flow, minimizing concentration and temperature gradients. The purpose of this numerical study is to optimize the geometric features of the reactor (injection nozzle diameters and length, and outlet pipe diameter) to improve the gas recycle ratio. Its hydrodynamic behavior is predicted by using multi-fluid solver, with an immersed boundary method to model the injector and easily vary its geometry. The effects of the operating parameters such as the injection flowrate, the pressure and the temperature are also assessed. In addition, a residence time distribution analysis allows for the evaluation of the Péclet number as a function of the geometric and operating parameters of the reactor. Then, a zero-dimensional hydrodynamic model, based on a macroscopic momentum balance, is finally developed. After fitting specific terms thanks to separated numerical CFD simulations, it enables a rapid optimization of the reactor design and provides insights into its behavior.

1. Introduction

In the actual climate change context, hydrogen appears to be a good candidate to help decarbonating the energetic mix while decreasing the energy production costs. One of the most used production processes is based on electrolysers: electricity is provided by renewable energy sources which allows water electrolysis and production of hydrogen and oxygen streams (Nasser et al., 2022). However, the electrolysis at industrial scale requests purification steps of the produced hydrogen and oxygen streams since the hydrogen one may contain a few percent of oxygen, and reciprocally, some hydrogen may be present in the oxygen one. This limits their valorization and may even imply some safety concerns (Kim and Kim, 2019).

In this context, the ConvCatH2 project was financed by RHyO Occitanie (France) to investigate the catalytic hydrogen conversion. One of the objectives of the project is to develop a kinetic reactor to perform this study.

For the kinetic study of catalytic gas-solid reactions, small-sized fixed beds operated in a once-through configuration (Kim et al., 2021), or short monoliths with wash coated channels (Hoek et al., 2004; Tahir and Amin, 2013), can be used. However, as species concentrations usually vary along the catalytic section, a differential model is needed to describe the reactor behavior and predict the outlet reaction yield. What is more, another issue lies in the possible radial and/or axial temperature gradients in the catalytic zone, that makes difficult data analysis. Conversely, recirculating fixed beds – or monoliths – can be considered isothermal and gradientless, provided the recycle ratio is high enough, allowing the catalytic reaction rate to be determined simply from the outlet stream composition (Fuchs and Hahn, 1993). There are several possible designs to achieve an efficient mixing within a catalytic reactor fed by a gas phase, such as the spinning basket reactor (Carberry, 1964), the axial flow impeller stirred reactor in which catalytic particles are fixed between gauzes in blade openings (Borman et al., 1994), the vibration mixed reactor (Hulburt, 1975), or the so-called Berty-type reactor. The latter, often use for kinetic studies, is based on an internal gas recirculation as described in (Cui et al., 2022). In the present study, an external recirculation system driven by inlet gas momentum is

* Corresponding author.
E-mail addresses: ronny.gueguen@toulouse-inp.fr (R. Gueguen), herve.neau@imft.fr (H. Neau), william.benguigui@edf.fr (W. Benguigui), annemarie.billet@toulouse-inp.fr (A.-M. Billet), carine.julcour@toulouse-inp.fr (C. Julcour), renaud.ansart@toulouse-inp.fr (R. Ansart).

https://doi.org/10.1016/j.cherd.2025.04.019
Received 14 January 2025; Received in revised form 29 March 2025; Accepted 11 April 2025
Available online 14 April 2025
0263-8762/© 2025 The Author(s). Published by Elsevier Ltd on behalf of Institution of Chemical Engineers. This is an open access article under the CC BY license (http://creativecommons.org/licenses/by/4.0/).

Nomenclature

Greek letters

ΔP_{aspi}	Pressure variation due to the aspiration (Pa)
ΔP_{bend}	Pressure drop across the bend containing the injection nozzle (Pa)
ΔP_{cat}	Pressure drop across the catalyst chamber (Pa)
$\Delta P_{jetloop}$	Pressure variation between recycle and jet-loop sections (Pa)
μ_{air}	Air viscosity (kg/m^{2}s)
ρ_{air}	Air density (kg/m^3)
τ_r	Recirculation rate (-)

Latin letters

$D_{inj,I}$	Inside diameter of the injection nozzle (m)
$D_{inj,O}$	Outside diameter of the injection nozzle (m)
$D_{out,i}$	Inside diameter of the outlet pipe (m)
D_t	Inside diameter of the reactor tube (m)
$E(t)$	RTD function (-)
H_{inj}	Penetration length of the injection nozzle inside the reactor (m)
$\dot{m}_{inj}$	Injected mass flow rate (kg/s)
$\dot{m}_r$	Recirculation mass flow rate (kg/s)
P	Pressure (Pa)
Pe	Péclet number (-)
P_{out}	Pressure applied at the outlet of the reactor (Pa)
S	Cross-sectional area relative to the subscript (m^2)
T	Temperature (K)
v	Gas cross-sectional averaged velocity (m/s)

Subscripts

inj	Relative to the gas injection
j	Relative to the jet-loop section
r	Relative to the recirculation section
t	Relative to the main reactor tube

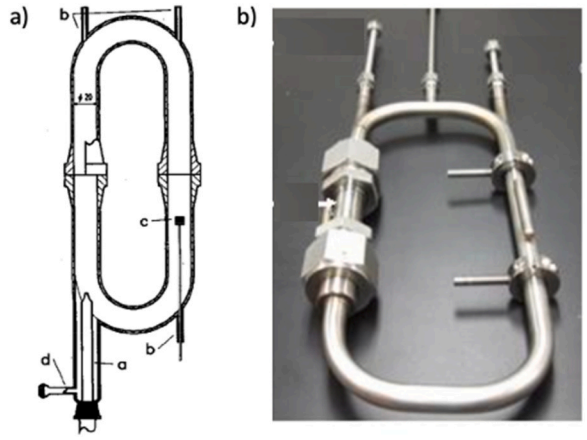

Fig. 1. a) Catalytic reactor with external recirculation loop proposed by (Fuchs and Hahn, 1993), and b) derived version, so-called "jet-loop" reactor (Nagaraj and Mills, 2013).

applied, where the gas is injected at high velocity through a nozzle located in the recycle loop. (Fuchs and Hahn, 1993) showed that such an external recirculation allows a better understanding of the gas velocity around the catalyst particles, a wide operating domain and the absence of metallic debris from the agitating external source. Furthermore, it can be more efficient in terms of mixing behavior. Then, they proposed their own reactor design (Fig. 1a). More recently, (Nagaraj and Mills, 2013) derived their jet-loop reactor from the previous one, but with the gas inlet and outlet located on each side of the reactor as illustrated in Fig. 1b. In the latter, the gas is injected thanks to a nozzle that penetrates within the main tube of the reactor (right part), then circulates through the fixed bed – the catalyst chamber – settled at the opposite side of the injection (left). Here, the resultant stream flow is separated: the first part flows out of the reactor, while the other part recycles within the reactor and is mixed with the injection. Both the recirculation rate – i.e. the ratio of the recirculation mass flowrate by the injected one – and the gas velocity inside the reactor are responsible of the efficiency of the latter (Fuchs and Hahn, 1993), since the gas velocity through the fixed bed must be high enough to ensure negligible heat and mass transfer resistance around the catalytic particles. However, the hydrodynamics in the reactor is linked to all the geometric and operating parameters.

The aim of this paper is to design a gas-phase reactor with significant recycle flow, starting from the jet-loop reactor geometry proposed by (Nagaraj and Mills, 2013), in order to accurately evaluate experimentally the kinetics of catalytic hydrogen conversion. To do so, 3D numerical simulations are used to investigate the hydrodynamics of such a reactor using *neptune_cfd* code, and to find the optimal key geometric parameters in regard with the recycle ratio. In the next section, the code itself and the models used are presented, followed by the description of the simulations set-up used to perform the parametric study described afterwards. Finally, a zero-dimensional hydrodynamic model is developed in order to provide an easy-to-handle tool that demands low computing time for the design of jet-loop reactors. Indeed, once the actual jet-loop device is built, experimental work will be performed to investigate the kinetics of the catalytic conversion of hydrogen in air, and test new catalysts. To efficiently define the range of operating conditions for this kinetic study, it will be necessary to model the hydrodynamics inside the jet-loop reactor for various temperatures, pressures, catalyst amounts, and gas phase compositions. For this step of the work, the 0D model will allow to save time by avoiding the numerous corresponding CFD simulations, which are time consuming.

2. Simulation description

This section describes the simulation procedure for the parametric study: the CFD (Computational Fluid Dynamics) code and related models, the jet-loop reactor geometry and its meshing, the numerical set-up and the result data post-processing.

2.1. Numerical background

2.1.1. neptune_cfd code

neptune_cfd code is developed by a consortium – EDF (*Electricité de France*), CEA (*Commissariat à l'Energie Atomique et aux Energies Alternatives*), Framatome and IRSN (*Institut de Radioprotection et de Sureté Nucléaire*) – in the framework of the NEPTUNE project to perform three-dimensional numerical simulations (Guelfi et al., 2007).

The solver is based on an Eulerian n-fluid approach, using pressure correction to simulate multiphase flows by solving a set of three balance equations for each phase. Turbulent polydisperse gas-solid flows models have been implemented in the code by the IMFT (*Institut de Mécanique des Fluides de Toulouse*) and the LGC (*Laboratoire de Génie Chimique*), extending its use to multiphase flows (Ansart et al., 2017; Deng et al., 2021). High performance computing simulations can be performed, making the code useful to design processes at high scale while keeping good resolutions (Neau et al., 2020, 2024). Details about the models

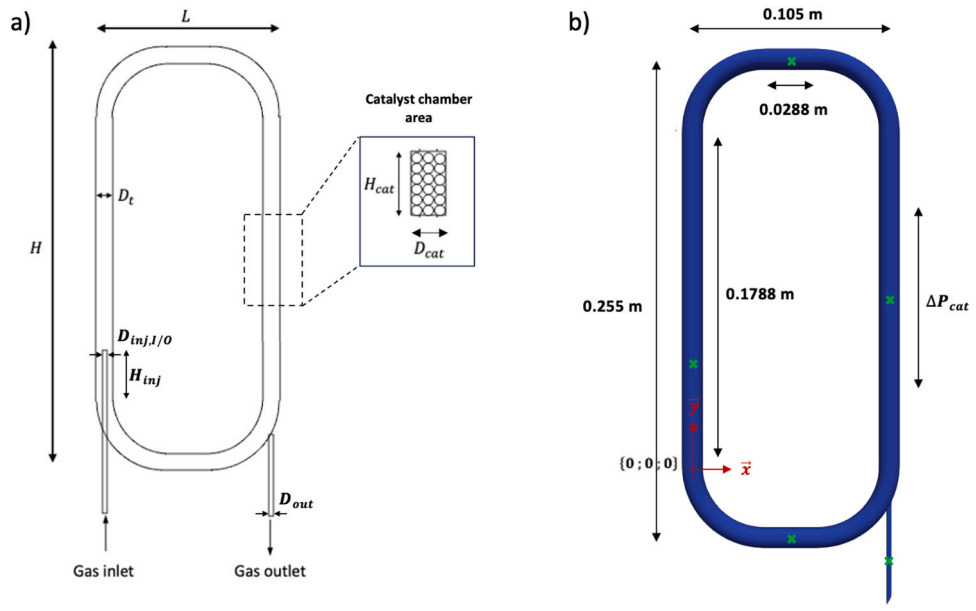

Fig. 2. a) Schematic representation of the jet-loop reactor and the dimensions of interest, and b) geometry representation for CFD simulations. The positions of the virtual probes – presented in Table 2 – are indicated by green crosses.

used by the *neptune_cfd* code can be found in the previously cited papers.

2.1.2. Physical and numerical models

The transport equations used by *neptune_cfd* are conventional (mass and momentum balances) and described in (Neau et al., 2020). The present case deals with a single-phase configuration with non-compressible flow, and the studied problem is considered as unsteady. Furthermore, the k-ε turbulence model is used to accurately describe the injection flow, even if the flow in the main reactor is laminar based on the involved velocities.

Concerning the phase properties, the fluid phase is modelled as air, where the density ρ_{air} depends on temperature T and pressure P according to the ideal gas law (Eq.(1)). Its viscosity μ_{air} only depends on temperature as shown in (Eq.(2)) (Welty et al., 2014). In these equations, $M_{air} = 0.029$ kg/mol is the air molar mass, and $R = 8.314$ J/(mol. K) is the ideal gas constant.

$$\rho_{air} = \frac{M_{air} P}{RT} \tag{1}$$

$$\mu_{air} = 8.8848.10^{-15} T^3 - 3.2398.10^{-11} T^2 + 6.2657.10^{-8} T + 2.3543.10^{-6} \tag{2}$$

During the foreseen experimentations, the reactor will contain catalyst material stacked in fixed bed configuration in a dedicated chamber, as explained in Section 2.2 hereafter. Depending on the size of the particles $d_{p,cat}$, on the bed void fraction ε_{cat} and length H_{cat}, and on the superficial gas velocity v flowing through it, a corresponding pressure drop ΔP_{cat} is induced according to the Ergün relation as illustrated by Eq.(3) (Ergün, 1952). The *neptune_cfd* code enables to specify a singular pressure drop coefficient K_{cat} over a chosen volume within the domain with Eq.(4). In the following, this coefficient is varied to model relevant values of the corresponding catalyst pressure drop and its impact on the reactor mixing (see Section 3.2.8).

$$\frac{\Delta P_{cat}}{H_{cat}} = 151.2 \frac{\mu_{air}}{d_{p,cat}^2} \frac{(1-\varepsilon_{cat})^2}{\varepsilon_{cat}^3} v + 1.8 \frac{\rho_{air}}{d_{p,cat}} \frac{1-\varepsilon_{cat}}{\varepsilon_{cat}^3} v^2 \tag{3}$$

$$\Delta P_{cat} = K_{cat} \frac{1}{2} \rho_{air} v^2 \tag{4}$$

2.2. Numerical set-up

2.2.1. Geometry and sizing

The geometry of the simulated reactor is inspired by the work of (Nagaraj and Mills, 2013), and is schematically represented in Fig. 2a. The overall dimensions (height H and length L) have been chosen to settle the whole experimental reactor – including its instrumentation – in a furnace with dimensions of 56 cm × 40 cm, so that the operating temperature may be easily varied and controlled. Then, dimensions of $H = 25$ cm and $L = 10$ cm seem to be relevant. According to the reactor described in (Nagaraj and Mills, 2013), the main tube is half-inch internal diameter, i.e. $D_t \approx 1$ cm.

The catalyst chamber is of same internal diameter (D_{cat}) as the main tube and is 10.16 cm long (H_{cat}). It is placed on the same side as the outlet pipe and at the opposite side from the injection one, to ensure the establishment of the flow before it enters the chamber. The injection nozzle penetrates within the reactor as explained in the Introduction. The penetration length of the injector H_{inj}, its inner and outer diameters, called $D_{inj,I}$ and $D_{inj,O}$ respectively, and the inner diameter of the outlet tube $D_{out,i}$ is varied to determine the best design combination with respect to the flow hydrodynamics.

The resulting geometry is referred to as the reference one for the following computations, and is shown in Fig. 2b. The origin is identified in red in the figure. In the specific simulations where the catalytic chamber is considered, the latter is modelled as a porous zone to take into account the fixed bed contribution. The beads inside the chamber are not described, but a corresponding pressure drop is integrated in the CFD as a contribution corresponding to the Ergün equation, as explained in the previous section. More precisely, the *neptune_cfd* code applies a penalization in the momentum equation for each cell of the dedicated zone. Finally, the injection and outlet pipes are added after the meshing operation of the main loop, as detailed in the next section.

2.2.2. Meshing methods

Concerning the meshing, the tube section is defined as an o-grid geometry in order to represent the domain only with hexahedral cells (Deng et al., 2021). The latter provide an accurate flux calculation in multiphase flows and a satisfying numerical stability. The mesh is initially created to represent a gas injection of $D_{inj,I} = 0.80$ mm I.D. with at least two cells in the radial direction of the injection tube. In other

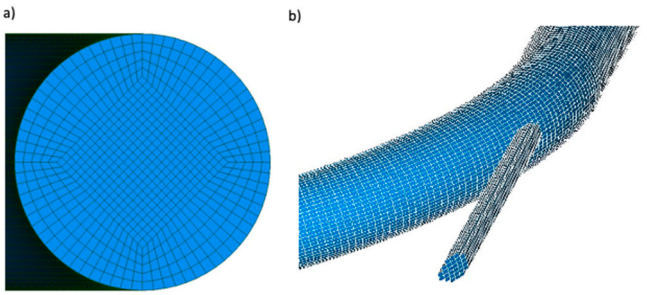

Fig. 3. a) Resulting sectional o-grid mesh, and b) extruded cells to mesh the outlet pipe.

words, the squared cells radial mean size at the center of the tube is $\Delta x = D_{inj,I}/2 = 0.40$ mm. Fig. 3a presents the resulting sectional mesh, with 28 cells within the tube diameter. In addition, the edges in the direction of the gas flow are discretized so that the resulting hexahedral cells have a size ratio of $\Delta y/\Delta x = 2$, since too elongated cells may induce numerical stability concerns. The mesh presented in this section has been selected following a mesh convergence study detailed in Section 3.1.2.

A non-negligible difficulty lies in the meshing of the gas injection pipe, whose geometry will be modified to optimize the reactor mixing, and of the boundary area between the latter and the main domain. Actually, one needs to divide the geometry, create blocks, groups of edges with the same number of elements and finally a multi-block mesh, respecting the edge constraints. Furthermore, it is very complicated to mesh such an injection pipe within a bend of the main reactor, for the same reasons. Then, very small cells will be created, especially at the injector boundary that will lead to very low time steps, which will increase the calculation times for each simulation. What is more, for each injector geometry tested, this complicated work has to be repeated, which is complex and time consuming. Hence, in this paper, a discrete forcing method developed by (Benguigui et al., 2018), inspired by immersed boundary methods (IBM) and called Time and Space Dependent Porosity (TSDP), is used to represent the gas injector and to easily change its geometry. The objective of this method is to model a solid body into the fluid field by associating a local porosity – between 0 for the solid phase and 1 for the fluid phase – while strictly ensuring the mass and momentum balance equations at the close vicinity of the interface. By reshaping the cells crossed by the interface, which is defined by either a geometric equation or from a CAD (Computer Aided Design) interpolation on the mesh, it is possible to build specific terms related to the immersed structure, to be like a body-fitted mesh. However, as the interface is locally approximated as a plane, it requires sufficiently fine spatial discretization for accurate representation. To model the interaction between the fluid and the immersed structure, face porosities are defined based on the finite volume theory and on the cell solid fraction, along with solid face properties such as their center of gravity and normal vector. These elements allow for the discrete integration of the wall effects, including diffusive terms that account for the presence of the solid face with a velocity computed thanks to a wall law and the pressure gradient. Thus, a recognition function is built to non-explicitly represent complex geometries, such as the injector here, inside the calculation domain without the need for complex mesh generation. This method, which is described in more details in (Benguigui et al., 2018), was used to perform Fluid Structure Interaction (FSI) simulations (Baraglia et al., 2021; Benguigui et al., 2019) for hydraulic applications (Benguigui et al., 2024) or offshore wind turbine applications (Benguigui and Peyrard, 2024; Rongé et al., 2023).

Finally, the outlet pipe is manually meshed by extruding cells from the main loop that correspond to the desired pipe diameter $D_{out,i}$, while keeping the same Δy cell size as in the main domain. Here, the objective is to avoid meshing the interface between a cylinder and a curved part of another cylinder. The example proposed in Fig. 3b corresponds to $D_{out,i} = 3.17$ mm. The corresponding whole mesh has a total of 561 276 hexahedrons for all the reactor.

Table 1
Operating and geometric parameters and their ranges for the simulations, as for the reference case of the study.

Parameter		Range	Reference Case
Injection	**Inner diameter $D_{inj,I}$**	0.40 – 2.50 mm	1.59 mm
	Outer diameter $D_{inj,O}$	1.59 – 6.40 mm	3.17 mm
	Penetration length H_{inj}	−0.010 – 0.075 m	0.050 m
	Injection mass flowrate $\dot{m}_{inj}$	1.10^{-6} – $1.2.10^{-4}$ kg/s	$1.2 * 10^{-4}$ kg/s
Outlet	**Inner diameter $D_{out,i}$**	0.80 – 3.17 mm	3.17 mm
	Outlet pressure P_{out}	1 – 15 bar	1 bar = 101 325 Pa
Catalyst pressure drop coefficient K_{cat}		0 – 15 500	0
Temperature T		300 – 600 K	300 K

Table 2
Localization of the probes in the domain.

Probe name	Position	Coordinates		
		x (m)	y (m)	z (m)
Inlet	*Downstream the injection pipe*	0	0.052	0
Top	*Top part of the reactor*	0.053	0.22	0
Cata	*At the catalyst chamber position*	0.11	0.05	0
Recycle	*Bottom part of the reactor – to detect recirculation*	0.05	−0.034	0
Outlet	*At the outlet of the reactor*	0.11	−0.04	0

2.2.3. Boundary conditions

The reactor outlet is a free outlet with imposed pressure P_{out} which is varied for some of the simulations to understand its influence on the hydrodynamics.

Since the injection pipe – which the geometry varies – is modeled by the time and space dependent porosity method, there is no conventional pressure nor velocity inlet related to this geometry. Instead, the gas injection is implemented by adding a momentum source term – the injection mass flowrate $\dot{m}_{inj}$ – in the balance equations within a zone corresponding to the inside part of the injector nozzle.

Finally, a non-slip condition is imposed for the walls.

2.2.4. Simulation procedure

The main objective of this study is to understand the influence of the operating and geometric parameters on the hydrodynamics of the jet-loop reactor, in order to design the latter for the experimental evaluation of the catalytic hydrogen conversion kinetics. The varying parameters and their ranges are listed in Table 1, and those selected for the reference case are detailed.

Several mesh sizes are used depending on the injector internal diameter (see next section). Numerical simulations have been carried out using 48–192 cores, on two supercomputers: Irene at TGCC (Très Grand Centre de Calcul du CEA) and Adastra at CINES (*Centre Informatique National de l'Enseignement Supérieur*). The time step for the simulations is adaptive and varies between approximately 10^{-4} and 10^{-6} s, depending on the other parameters, to ensure that the Courant and Fourier numbers are less than 1 and 10, respectively. The physical time simulated varies depending on the other parameters to make sure the flow is established (with stabilized pressures and velocities), that corresponds to calculation times ranging between 1 and 10 days. The numerical methods used by *neptune_cfd* are further described in (Neau et al., 2020).

For each simulation, pressure and velocities are initialized at value 0 throughout the domain.

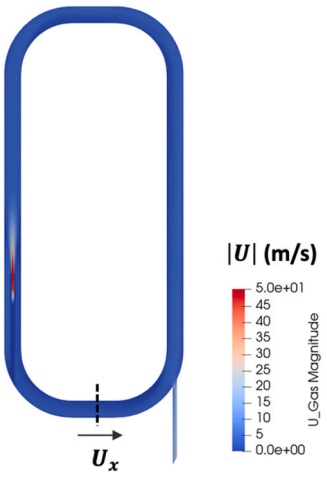

Fig. 4. Contour of velocity magnitude for the reference case, with a z-axis cut section.

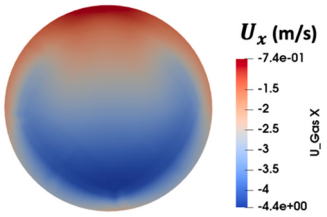

Fig. 5. x-axis cut section of the U_x velocity field (at the position of the recirculation probe) that highlights the recirculation.

Several fictitious probes have been implemented within the domain to record quantities of interest along physical time. Their positions are detailed in Table 2, along with their Cartesian coordinates according to the origin position (cf. Fig. 2b).

3. Results

3.1. Reference case

The reference case is defined with the parameters specified in Table 1, and the mesh detailed in Section 2.2.2. The temperature is considered as uniform throughout the reactor and is set at 20°C, while atmospheric pressure (101,325 Pa) is imposed at the outlet. The pressure inside the domain is calculated at each node thanks to the balance equations, according to the injected mass flowrate (here of $1.2.10^{-4}$ kg/s). The intern and outern diameters of the injection nozzle are 1.59 and 3.17 mm, respectively, its penetration length within the jet-loop reactor is 0.05 m, and the intern diameter of the outlet pipe is 3.17 mm. For the reference case, the pressure drop through the catalytic bed is not modelled ($\Delta P_{cat} = 0$). It may correspond to the case where the jet-loop incorporates a short wash coated monolith piece as catalytic chamber: in that case, the pressure drop will be negligible.

3.1.1. Hydrodynamics of the reference case

Pressures and velocities are recorded by the probes as a function of the physical time. These quantities are quickly stabilized, in less than 0.5 second. Obviously, pressure and velocities are stronger in the gas injection zone than anywhere else in the domain, as it can be observed in Fig. 4 showing the z-axis cut section of the velocity magnitude contour at a time of 5 seconds. This is due to the high momentum of the injected gas.

The recirculation flow is caused by the high momentum (or energy) of the gas injected, which has to be sufficient to compensate all the pressure losses in the reactor, and in particular that resulting from the section shrinkage due to the presence of the injection tube within the main pipe. The latter implies a pressure drop but also a local increase in velocity, which induces the entrainment of the gas from the loop, as it will be highlighted in Section 4. To characterize the recirculation and thus the mixing, the corresponding quantity of interest is the recirculation rate τ_r (ratio of the recirculation mass flowrate $\dot{m}_r$ by the injection one (Eq.(5)). The recirculation flowrate is calculated by processing the CFD results and integrating the velocity U_x in the direction of the flow over the tube section (Eq.(6)), at the position of the associated probe. Fig. 5 shows the corresponding x-axis cut section of the longitudinal velocity field. The recirculation flow is highlighted by negative U_X velocities, while the asymmetry of the field is due to the centrifugal force (after a bend).

$$\tau_r = \frac{\dot{m}_r}{\dot{m}_{inj}} \tag{5}$$

$$\dot{m}_r = \rho_{air}\dot{q}_r = \rho_{air}\int_S -U_x dS \tag{6}$$

3.1.2. Mesh convergence

To determine the mesh influence, several meshes have been built that satisfactorily represent the gas injector for the different intern diameters considered of 0.40, 0.80, 1.20 and 1.59 mm, i.e. with two cells across the radial direction, in the same way as explained in the Section 2.2.2 for the mesh n°3. All the discretization schemes are deduced from this value, leading to meshes with various cell sizes in the main tube section, as shown in Fig. 6 and described in Table 3. They were used to perform mesh convergence test-simulations for the reference case of the reactor (same configuration with intern diameter of $D_{inj,I} = 1.59$ mm).

The conventional method to evaluate the mesh influence is to plot a relevant quantity regarding the hydrodynamics as a function of the number of cells. Despite the relevance of the recirculation rate τ_r, it does not account for the numerical injection surface ($S_{inj,I,num}$) that actually varies depending on the mesh used. Then, the selected quantity is not only the recirculation rate (i.e. the ratio between the mass flow rates at the recirculation by the injection), but the ratio of the flow forces, denoted F, which are actually the time derivative of the momentum in stabilized flow. Thus, one can express the ratio of the momentum at the recirculation by the momentum at the injection, involving the corresponding mass flowrates ($\dot{m}_r$ and $\dot{m}_{inj}$) and the associated numerical

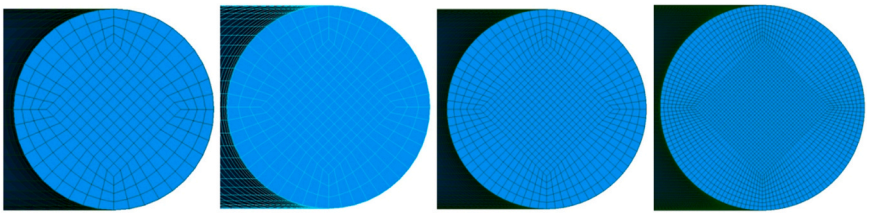

Fig. 6. Cross-sections of the computed meshes, to model an injector internal diameter of 1.59 mm, 1.20 mm, 0.80 mm and 0.40 mm (from left to right), each with two cells across the radial direction.

Table 3
Meshes parameters.

Mesh number	Number of cells	Cell radial size at the center of the tube Δx (mm)	Cell surface (m^2)	Cumulated cell surface to model the injector nozzle (from $D_{inj,I} = 1.59$ mm)	Momentum ratio ($\frac{F_r}{F_{inj}}$, Eq.(7))
1	77 520	0.79	$2.68.10^{-7}$	$7.4.10^{-7}$	0.010
2	157 752	0.60	$1.86.10^{-7}$	$1.07.10^{-6}$	0.111
3 (reference case)	561 276	0.40	$8.3.10^{-8}$	$1.32.10^{-6}$	0.149
4	4 261 696	0.20	$2.1.10^{-8}$	$1.57.10^{-6}$	0.155

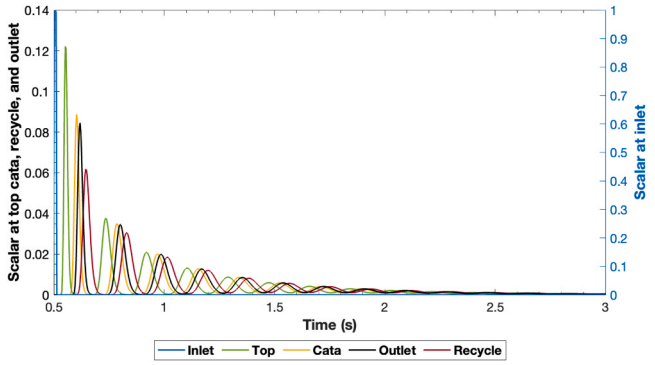

Fig. 7. Time evolution of the tracer recorded by several fictitious probes in the reactor.

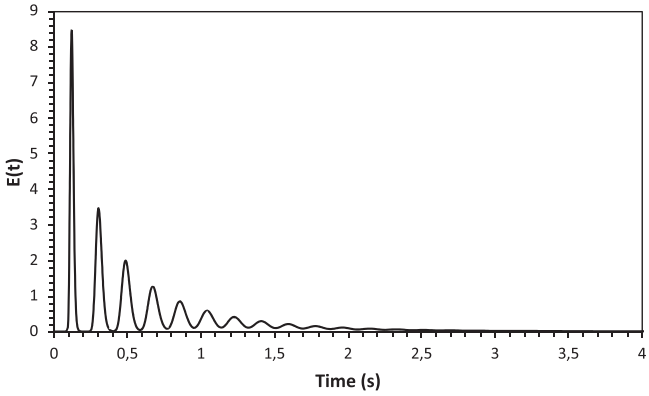

Fig. 8. Residence time distribution function of the reference case.

surfaces, respectively $S_{t,num}$ and $S_{inj,I,num}$. This new quantity which accounts for the various meshes is defined by Eq.(7), and its evolution versus the number of cells is indicated in the right column of Table 3, where the mesh convergence is highlighted (see Appendix A for more details). Furthermore, the results provided by the 561 276 cells mesh (n°3) seem to match those obtained with the most refined mesh. As a compromise between precision and calculation time, this intermediate mesh is conserved. For this selected grid, cell dimensions vary from 0.4 mm (in the squared part of the grid) to 0.7 mm (at the edge of the grid), and the cell axial length is twice the minimum one as explained in dedicated Section 2.2.2, i.e. 0.8 mm.

$$\frac{F_r}{F_{inj}} = \frac{\dot{m}_r v_r}{\dot{m}_{inj} v_{inj}} = \frac{\dot{m}_r{}^2}{\dot{m}_{inj}{}^2} \frac{S_{inj,I,num}}{S_{t,num}} \tag{7}$$

3.1.3. RTD analysis

According to (Fuchs and Hahn, 1993), the single value of the recycle ratio is not sufficient to conclude that the reactor is well-mixed. Thus, a residence time distribution (RTD) analysis was also performed. To do so, a scalar was injected as a pulse signal from 0.5 to 0.51 second, i.e. over a time corresponding to nearly 1 % of the residence time in the reactor after the flow has been stabilized (Gamba et al., 2012).

Fig. 7 depicts the scalar value recorded by all the probes of the domain as a function of time. On this figure, the gas trajectory can be followed from probe to probe: first the scalar is injected at the inlet as a sharp peak, whose concentration is given by the right axis (blue curve), then the scalar is detected at the top of the reactor (green), and at the catalyst chamber position (yellow). It is then split into a fraction that goes through the outlet pipe (black curve), and a fraction that recirculates inside the reactor (red).

The classical RTD theory has been described for years in the literature for continuous reactor (Gamba et al., 2012; Levenspiel, 1972; Li et al., 2024). For well-mixed reactors, the shape of the outlet curve is a decreasing exponential. It corresponds actually to the envelop of the curves presented above, which characterize the residence time distribution of the gas within the reactor over all the loops. In the present configuration, the outlet curve shown in Fig. 7 (in black) is a succession of peaks, typical of a loop reactor with recycling flow (Battaglia et al., 1993; Melo et al., 2001; Yu and Shen, 2024). The spacing between the peaks is relative to travelling time for one loop, which is linked to the recirculation rate (i.e. the mixing level) in the reactor.

The continuous reactor analysis consists of calculating the RTD function $E(t)$ which – for a Dirac-type injection and a quasi-constant gas velocity at the outlet cross-section – is actually the normalized time evolution of the scalar concentration at the outlet of the reactor (Eq.(8)), with $C(t)$ the tracer concentration detected by the associated probe (Fig. 8). This curve can then be analyzed by determining its first and second moments, respectively $\bar{t}$ and σ^2. The former characterizes the mean residence time of the gas within the reactor (Eq.(9)), while the latter is the variance and represents the dispersion around $\bar{t}$ (Eq.(10)). For the reference case presented in this section, these moments are respectively $\bar{t} = 0.71$ s and $\sigma^2 = 0.44$ s^2. Note that the residence time is also calculated with the ratio between the reactor volume and the volume injection flowrate, and found to be 0.71 s too, which proves the consistency of this RTD study.

$$E(t) = \frac{C(t)}{\int C(t)dt} \tag{8}$$

$$\bar{t} = \int_0^\infty E(t).tdt \tag{9}$$

$$\sigma^2 = \int_0^\infty E(t).(t-\bar{t})^2 dt \tag{10}$$

The hydrodynamic model based on plug flow with axial dispersion is used, that enables to calculate a Péclet number Pe to characterize the mixing level of the reactor (Rastegar and Gu, 2017). The latter compares advection and dispersion levels in the considered flow. Thus, the lower the Pe value, the higher the mixing. To identify the Péclet number for gas flow in the jet-loop reactor, a relation derived from the moments of the $E(t)$ function with closed boundaries is used (Eq.(11)), which is relevant for tight sections at the inlet and outlet of the reactor (Trambouze and

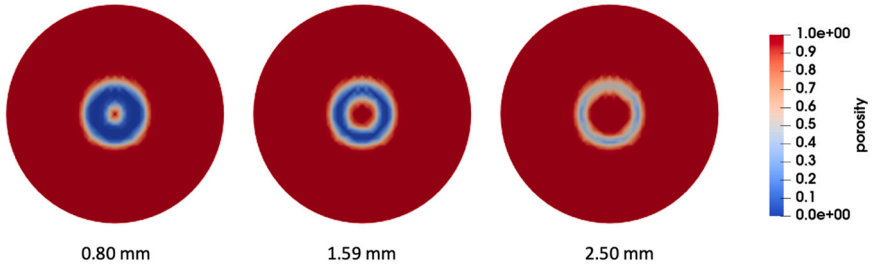

Fig. 9. Cross-sections of the main tube showing the injection pipe modelled with the TSDP method (in blue) for different inside diameter values.

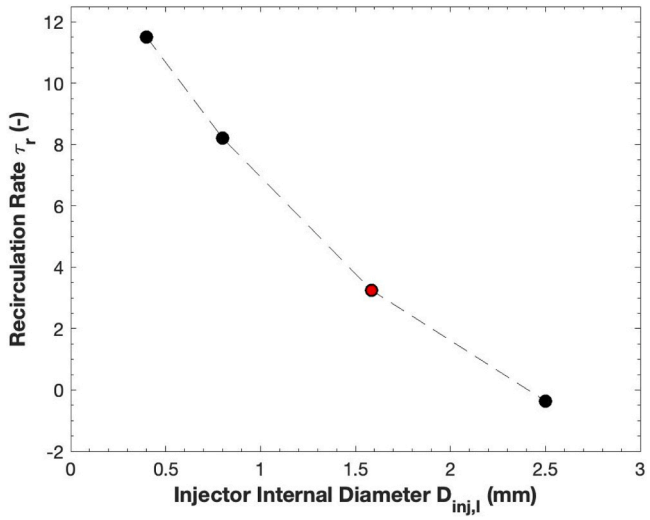

Fig. 10. Evolution of the recirculation rate as a function of the inside diameter of the injection nozzle, with the reference case highlighted in red.

Euzen, 2002). For the reference case, solving Eq.(11) leads to a computed value of $Pe = 2.99$. The RTD study hence complements the recirculation rate value as a characterization of the mixing quality and thus helps to design the jet-loop reactor.

$$\frac{\sigma^2}{\bar{t}^2} = \frac{2}{Pe} - \frac{2}{Pe^2}\left(1 - e^{-Pe}\right) \tag{11}$$

RTD results in terms of the Péclet number (when available) are presented in the next section, which focuses on the parametric study for reactor geometry optimization. In some cases, namely with a strong gas injection, the jet penetrates as far as the first elbow of the reactor, leading to special hydrodynamics. In addition, the associated calculation times being more than 10 days, these particular cases are not exploited in terms of RTD, but the recirculation rates are still relevant. However, the RTD cases presented in the parametric study still illustrate configurations with very different mixing levels, ranging by a factor of 5 in terms of recirculation rates.

3.2. Parametric study

The aim of this section is to understand the influence of the geometrical and operating parameters on the hydrodynamics, to determine an optimal configuration of the reactor for future kinetic experiments. These parameters are varied independently, based on the reference case (see Table 3). Their impact on the recirculation rate τ_r is assessed hereafter.

3.2.1. Inside diameter of the injection nozzle

The first investigated parameter is the inside diameter of the injection nozzle, $D_{inj,I}$. It is varied in a range of 0.4–2.5 mm, keeping the other

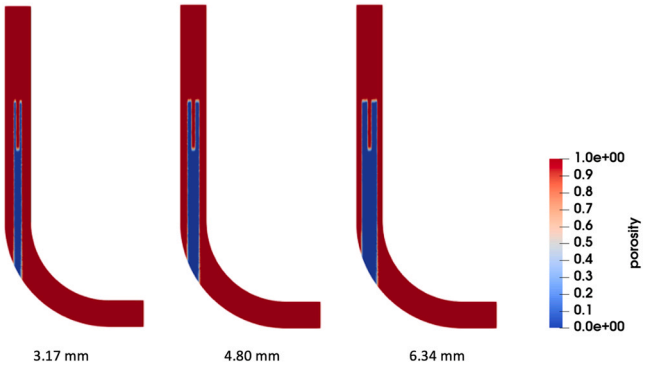

Fig. 11. Vertical cut-sections of the tube for different outside diameters of the injection nozzle (in blue).

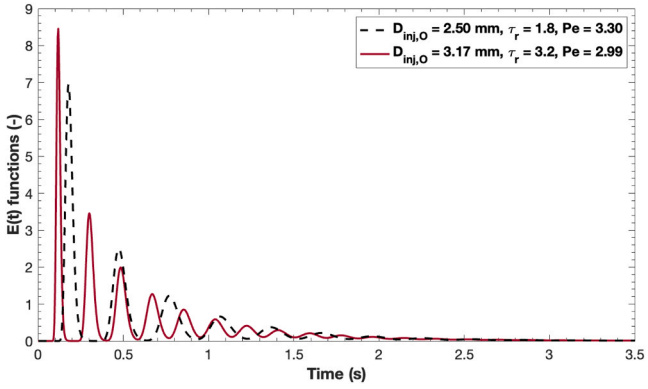

Fig. 12. RTD comparison between injector outside diameters of 2.50 mm (black) and of 3.17 mm (red).

parameters constant (at the values of the reference case). As explained in the previous sections, the injection pipe is modelled thanks to the time and space dependent porosity method (TSDP). The latter refines the concerned mesh to define a gas-solid interface and associates a porosity value to the cells, as shown in Fig. 9 with mesh cross-sections for various $D_{inj,I}$, where the injection nozzle is materialized in blue.

In Fig. 10, the recirculation rate τ_r is plotted as a function of $D_{inj,I}$. The other parameters being constant, the injection mass flowrate is kept at $1.02 * 10^{-4}$ kg/s, meaning that τ_r is proportional only to the recirculation mass flowrate ($\dot{m}_r$). In this figure, the reference case is marked in red. The recirculation rate strongly increases as the injector inside diameter is decreased. This is expected because the injected momentum is also increased.

Since $D_{inj,I}$ seems to be a critical parameter, further comparisons are made using the reference inside diameter (1.59 mm) and an intermediate value of 0.80 mm for the rest of the parametric study.

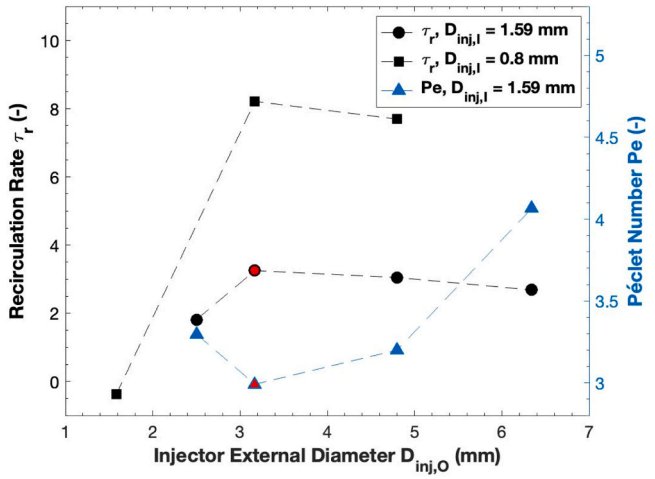

Fig. 13. Evolution of the recirculation rate (black) and of the Péclet number (blue) as a function of the injector outside diameter, with the reference case highlighted in red.

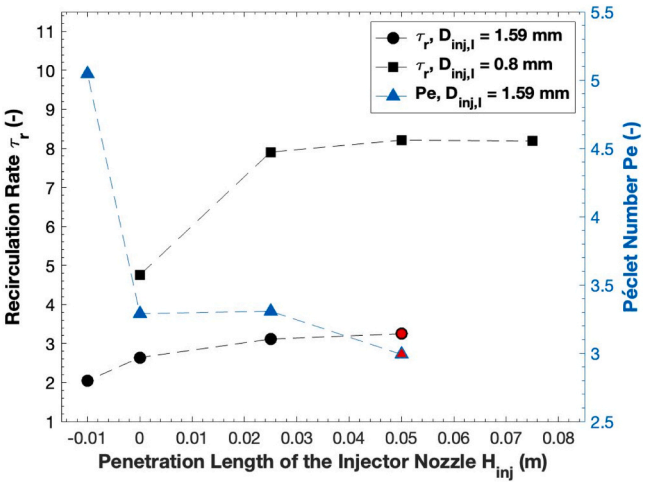

Fig. 15. Evolution of the recirculation rate (black) and of the Péclet number (blue) as a function of the injector penetration length, with the reference case highlighted in red.

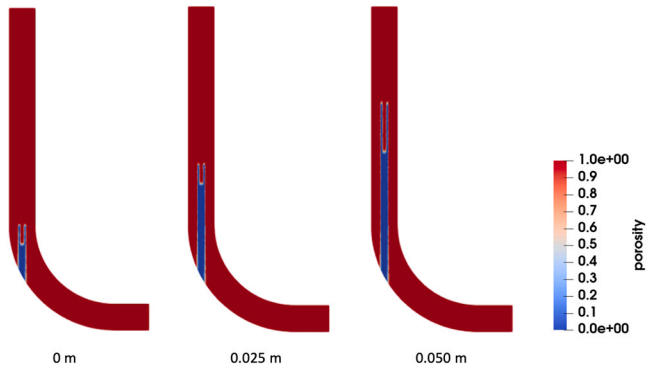

Fig. 14. Vertical cut-sections of the main tube showing the injection pipe (in blue) for different injector penetration length (H_{inj}) values.

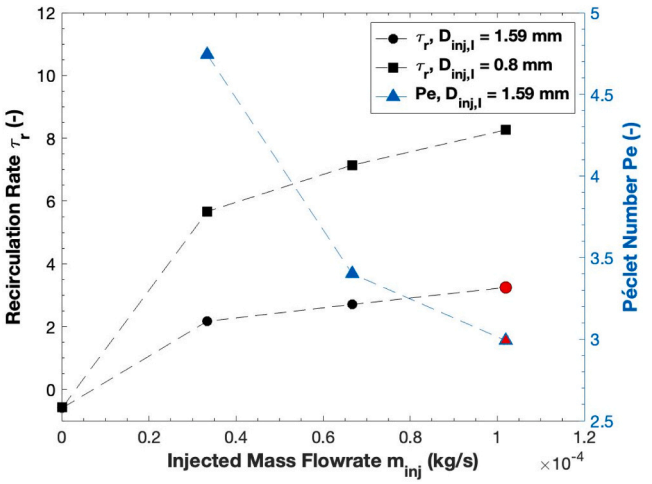

Fig. 16. Evolution of the recirculation rate (black) and of the diffusion coefficient (blue) as a function of the injected mass flowrate, with the reference case highlighted in red.

3.2.2. *Outside diameter of the injection nozzle*

The second parameter is the outside diameter of the injection nozzle, $D_{inj,O}$. This parameter is expected to have also a strong effect on the recirculation rate since it directly affects the cross-section offered to the recirculating flow around the injection pipe and thus the associated pressure drop. Values between 1.59 and 6.40 mm are tested, with inside diameters of 0.80 and 1.59 mm, as it can be seen in Fig. 11 with vertical cut-sections of the system.

Fig. 12 shows a comparison of the $E(t)$ functions calculated for outside diameter values of 2.50 mm (dashed black) and 3.17 mm (full red). One can observe that the red curve corresponds to a better mixing level, with a faster recirculation flow within the reactor loop, meaning a higher recycle rate and a lower Péclet number. These two quantities are plotted as a function of $D_{inj,O}$ in Fig. 13: the recirculation rate is marked in black for the two selected values of 1.59 mm (circles) and 0.80 mm (squares) of the injector inside diameter $D_{inj,I}$, and the Péclet number is plotted using blue triangles for the reference value of the inside diameter. The curves show an optimum in terms of τ_r and Pe for 3.17 mm O. D. whatever the inside diameter. Indeed, the presence of the outside wall of the injection pipe is responsible for the restriction in cross-section upstream from the injection point, thus inducing a flow acceleration and a suction phenomenon, while causing a higher pressure drop in this area too. The existence of an optimal value for $D_{inj,O}$ corresponds to a compromise between these two phenomena: the strong momentum injected through the nozzle, combined with the presence of the injection pipe, causes an aspiration of the flow coming downwards. Of course, if the injection pipe is too large, the induced pressure drop will be too high and there will be no recirculation.

3.2.3. *Penetration length of the injection nozzle*

Another parameter related to the gas injector is its height from the origin H_{inj} (cf. Fig. 2b), i.e. the penetration length of the injection nozzle inside the reactor. The set value varies between −0.010 and 0.075 m. Fig. 14 illustrates various H_{inj} values on vertical cut-sections.

Then, Fig. 15 presents the evolution of the recirculation rate as a function of H_{inj}. The recirculation rate reaches a maximum value when H_{inj} lays between 0.050 and 0.075 m, regardless of the injector inside diameter. This value is confirmed by the Péclet number trend. This was also expected since the injected momentum can't suck in gas and induce the recirculation if it is introduced too close to the reactor outlet. However, if it is too far away, there would be too much friction of the recirculated gas along the injection pipe and this would decrease τ_r.

3.2.4. *Injected mass flowrate*

The injected mass flowrate $\dot{m}_{inj}$ is varied between 10^{-6} and $1.02 * 10^{-4}$ kg/s. Consequences are shown in Fig. 16 for the recirculation rate (black) and the Péclet number (blue). The former increases

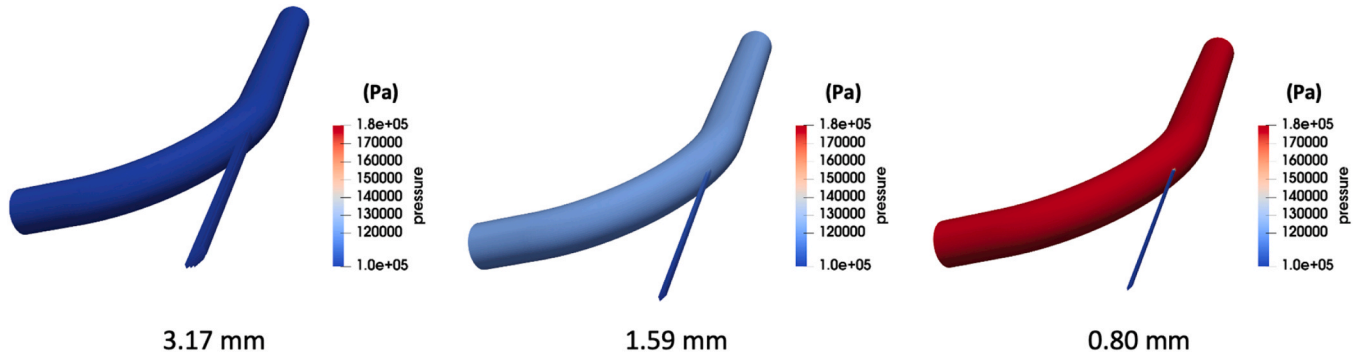

Fig. 17. Representation of different outlet pipe diameters, colors corresponding to the pressure field in Pascal.

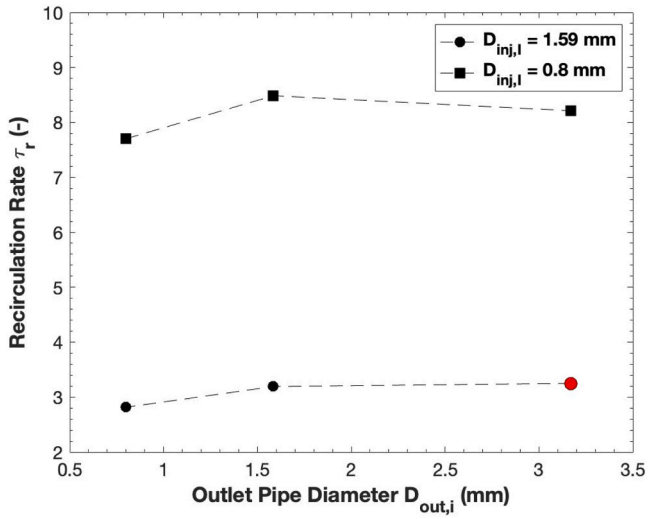

Fig. 18. Evolution of the recirculation rate as a function of the outlet pipe diameter, with the reference case highlighted in red.

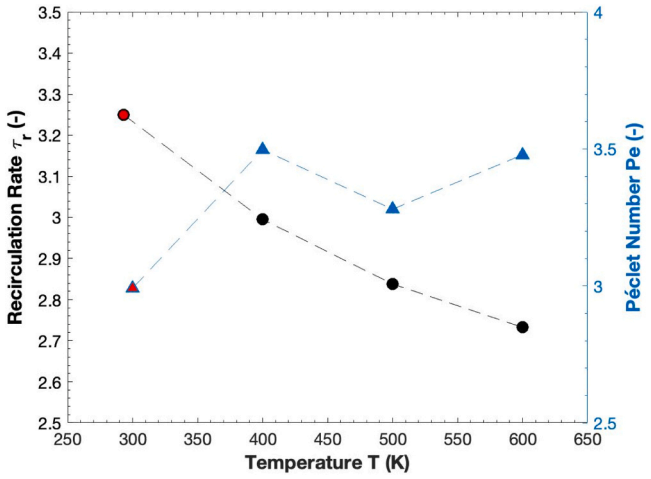

Fig. 19. Evolution of the recirculation rate (black) and of the Péclet number (blue) as a function of the temperature, with the reference case highlighted in red.

while the latter decreases with $\dot{m}_{inj}$, which was expected because it increases the momentum quantity injected. Since it does not impact the geometric design of the reactor, the injected mass flowrate will be an operating parameter that will freely vary during the kinetic study of the reaction, in a range that enables to keep a high mixing level.

3.2.5. Outlet pipe diameter

The outlet pipe of the reactor is focused next. The first parameter of interest is its inside diameter, $D_{out,i}$. To vary it, the procedure explained in Section 2.2.2 is used, extruding cells that correspond to the wished $D_{out,i}$. With atmospheric pressure imposed at the outlet, the pipe creates a pressure drop that varies the pressure inside the reactor. The latter logically increases when decreasing the outlet diameter, as highlighted in Fig. 17 with pressure fields for three values of $D_{out,i}$.

Depending on the pressure increase in the reactor caused by the reduction of $D_{out,i}$, the gas density can also be impacted since the mass flow rate is imposed (cf. Eq.(1)). To take into account this possible modification, calculations have been run using compressible flow models with *neptune_cfd*. It should be noted that this greatly increases the calculation time, hence the Péclet numbers are not given here for the same reasons as previously mentioned. Results are shown in Fig. 18 in terms of recirculation rate versus outlet pipe diameter, for two injector internal diameters. An optimum configuration appears for an outlet pipe of around 1.5–2 mm. Actually, the reduction of the pipe section is useful because it keeps a large amount of the gas flow inside the reactor. On the other hand, a tight reduction induces a high pressure drop and slows down the outlet gas flow. However, it can be emphasized that the variations of τ_r are very low compared to those previously presented.

3.2.6. Pressure and temperature

The imposed pressure P_{out} has been assessed following the same idea as above, using compressible flow models for the calculation. The corresponding results are not presented here to avoid overloading since the recirculation mass flowrate remains constant. Actually, for a constant injected mass flowrate at increasing pressure, the increase in gas density offsets the velocity decrease so that the advection term is not impacted, hence the recirculation neither. This assessment allows the operating pressure to be freely varied during the kinetic study without impacting the mixing level.

The temperature influence is assessed by modifying the air density and viscosity accordingly, as described in Section 2.1.2 (Eqs.(1) and (2), respectively). Fig. 19 reveals the consequences of such changes in gas properties on the recirculation rate and the Péclet number in the same way as previously done. The simulation results show the increase in temperature decreases the mixing, as previously observed by (Fuchs and Hahn, 1993) in their jet-loop reactor. This is actually due to two opposite effects: as the injected mass flowrate is constant, the decrease of the density with temperature increases the gas velocity, that is counterbalanced by the increase of viscosity, finally leading to a recirculating mass flowrate decrease.

Nevertheless, the variations are relatively low (relative variation of less than 20 %), so that temperature variations during the experimental campaign should not significantly affect the hydrodynamic behavior of the reactor.

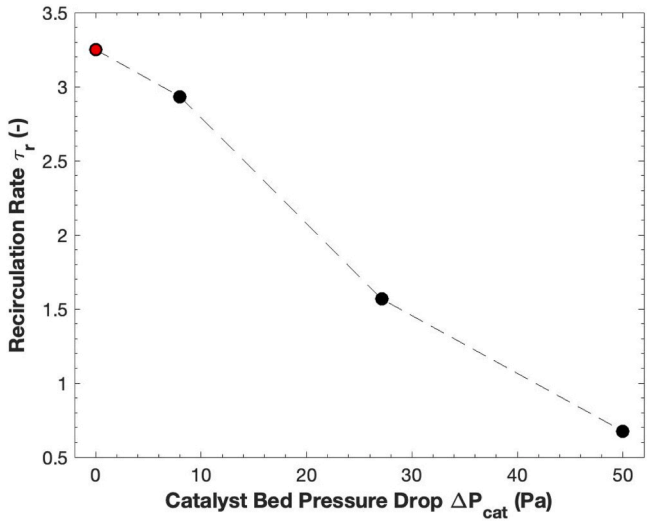

Fig. 20. Evolution of the recirculation rate as a function of the pressure drop through the catalyst bed, with the reference case highlighted in red.

3.2.7. Catalyst bed

As explained in Section 2.1.2, the pressure drop corresponding to the catalyst bed (ΔP_{cat}) could be modelled by Eq.(4) by setting a representative value for the corresponding coefficient K_{cat}. However, the actual pressure drop coefficient in the fixed bed depends on the velocity of the gas flowing through the catalyst, which in turn depends on the catalyst properties and the recirculation rate, that is itself affected by the pressure drop across the fixed bed. Then, values of K_{cat} are imposed to induce relevant fixed bed pressure drop, as presented in Fig. 20 with respect to the recirculation rate.

It can be seen in Fig. 20 that, as expected, the higher the pressure drop, the lower the recirculation rate, meaning that it decreases the mixing level inside the reactor up to almost no recirculation when the pressure drop reaches 50 Pa. This pressure drop value is realistic since it corresponds to a 1.5 cm length of the catalyst chamber (H_{cat}), according to the Ergün's equation (cf. Eq.(3)) and considering 3 mm particles with 0.4 bed void fraction.

The catalyst chamber impacts the lateral distribution of the gas velocity, as highlighted in Fig. 21 with radial profiles of the axial gas velocity over the tube cross-section, upstream (black) and downstream (red) the catalyst chamber, for the same case as above. First, one can observe the asymmetry due to the singularity created by the bend upstream the chamber (because of the centrifugal force, as shown in Fig. 6). Second, the red full line recorded just at the outlet of the chamber (y = 0.02 m) highlights the radial homogenization of the axial gas velocity due to the fixed bed, proving that the latter is well modeled. However, this disturbance vanishes before the flow reaches the next bend in the main tube, as shown by the red dashed curve in the figure (y = 0 m) where the flow radial profile recovers a Poiseuille shape. Hence, it does not impact the recirculating flow.

3.3. Reactor design

According to the parametric study presented above regarding both the recirculation rate τ_r and the Péclet number *Pe*, an improved design for the jet-loop reactor can be determined. Table 4 summarizes the values of the associated geometric parameters. This design actually corresponds to the case presented in Fig. 10 with $D_{inj,I} = 0.4$ mm, but with a smaller outlet diameter $D_{out,i}$. Since we presented in the previous section the low influence of the latter, one can expect a recirculation rate τ_r of around 12 with this improved design.

These values were adjusted to manufacture an experimental device. A simulation was then performed with the adapted geometric parameters detailed in Table 4, that results in a recirculation rate of 9.1 without catalyst chamber. The latter has been implemented considering a catalyst pressure drop ΔP_{cat} of 50 Pa as in the previous section, that decreases τ_r to 8.3 which corresponds to an acceptable level of mixing. According to these observations, in experimental conditions, the amount of catalyst will have to be carefully adapted to the quantity required to study the kinetics as it strongly affects the reactor mixing.

4. Zero-dimensional hydrodynamic model

A drawback of the CFD parametric study presented in the previous section is that it is time consuming and involves much computing resources. Then, this section is dedicated to the development of a zero-dimensional hydrodynamic model based on pressure drop balances fed by 3D numerical simulation as an easy tool for the design of a jet-loop reactor.

4.1. Model considerations

The basis of the model is a force balance between two cross-sections of the reactor, i.e. (i) just below the entrance to the bend where the injection nozzle is embedded, and (ii) downstream from the injection, where the injected flow and the recirculated flow merge. These two

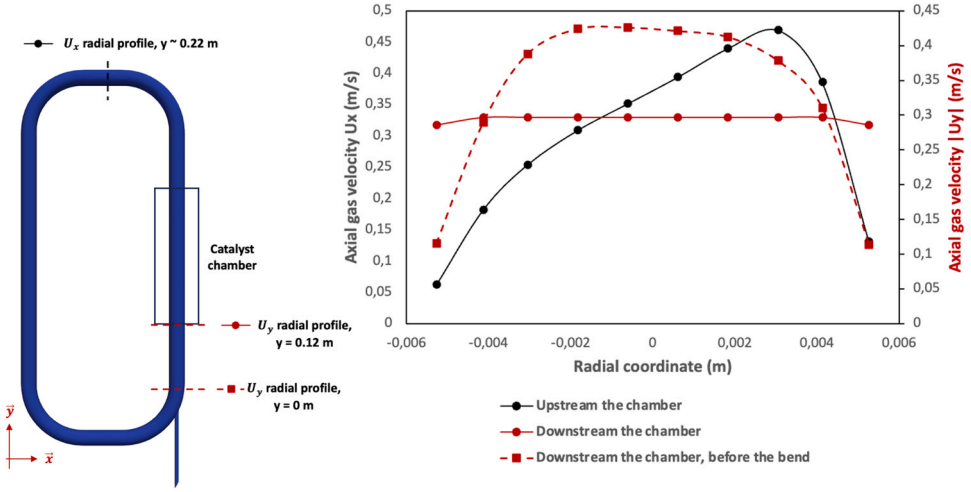

Fig. 21. Radial profiles of the gas axial velocity over the tube cross-section, upstream at y ~0.22 m (black) and downstream the chamber (red), at y = 0.02 m (full line) and 0 m (dashed line), for the case of the highest pressure drop in Fig. 22.

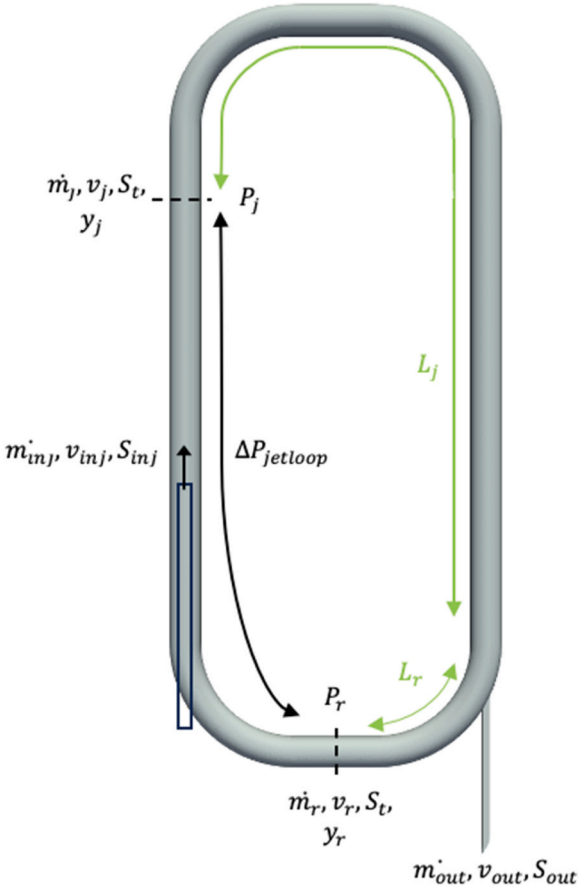

Fig. 22. Variables and parameters involved in the hydrodynamic 0D model.

Table 4
Geometric parameters of the optimized reactor according to the CFD study.

Parameter	Injection nozzle			Outlet pipe
	Inside diameter $D_{inj.I}$	Outside diameter $D_{inj.O}$	Penetration length H_{inj}	Inside diameter $D_{out.i}$
Improved design	0.40 mm	3.17 mm	0.05 m	1.59 mm
Manufactured experimental device	0.60 mm	3.17 mm	0.05 m	1.39 mm

cross-sections, further identified by the subscripts "r" for "recycle" and "j" for "jet-loop", are highlighted in Fig. 22 together with the involved variables. The positions of their centers are (-0.038,0.034) and (0,0.1) respectively, relative to the same origin as in the previous CFD study.

Eq.(12) corresponds to the projection of the steady state momentum balance in the direction of the flow axis, while considering the assumption of homogeneous gas velocity over the tube cross-section. This macroscopic balance relates the pressure force and momentum flowrate at the two abovementioned cross-sections to the pressure loss between these sections, $\Delta P_{jetloop}$. The latter is due to the viscous friction on the tube walls and to the cross-sectional irregularities (singular head losses), but it also includes the aspiration effect created by the injection in the left-hand part of the reactor, which drives the recirculation. Then, $\Delta P_{jetloop}$ can be decomposed into two terms, (Eq.(13)) where ΔP_{bend} is the friction contribution, while ΔP_{aspi} is the aspiration phenomenon contribution (and of opposite sign since it corresponds to an increase in pressure).

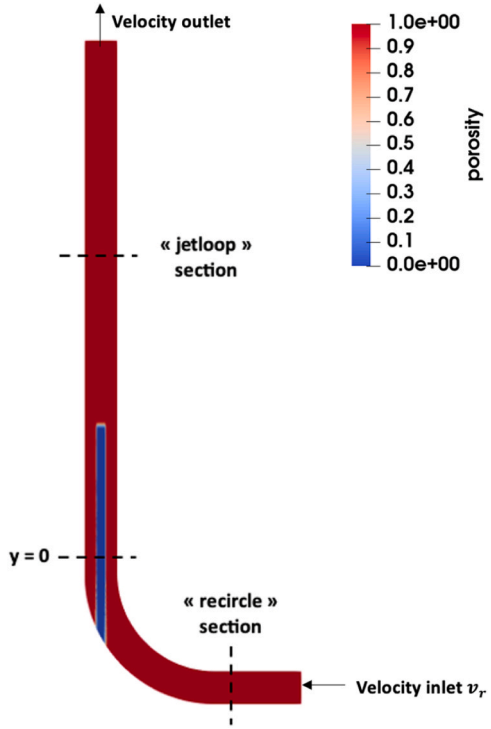

Fig. 23. Considered domain for the CFD study dedicated to the investigation of ΔP_{bend}, with the injection pipe in blue.

$$P_r S_t + \dot{m}_r v_r = P_j S_t + \dot{m}_j v_j + \Delta P_{jetloop} S_t \tag{12}$$

$$\Delta P_{jetloop,0D} = \Delta P_{bend} + \Delta P_{aspi} \tag{13}$$

For the right part of the loop, the contribution of the catalyst bed to $\Delta P_{jetloop}$ is not considered for direct comparison with the CFD results. The same applies to the contribution of the outlet tube since the CFD simulations demonstrated that its geometry does not significantly affect the recirculation rate (cf. Section 3.2.5). Finally, the calculation is also performed close to atmospheric conditions since the temperature and pressure have only a minor effect, as presented in the parametric study above.

4.2. Pressure drops expressions

4.2.1. ΔP_{bend} (left side of the loop)

To isolate the pressure loss due to the presence of both the bend and the injection pipe, another CFD study was performed with a domain including the considered area only, i.e. without the complete loop (Fig. 23). The mesh and all the simulations parameters are the same as before (see Section 3.2: parametric study of the jet-loop), the only difference laying in a gas velocity inlet imposed in the recirculation section.

Several values have been tested for the outside geometrical parameters of the injection pipe, i.e. its outside diameter $D_{inj,O}$ and penetration length H_{inj}, with the same ranges as previously mentioned. Furthermore, the inlet velocity v_r varies here from 0.1 up to 20 m/s to take into account a large variation range. In this case, the Bernoulli's equation can be applied (Bernoulli, 1738), which allows a direct calculation of the corresponding pressure drop (Eq.(14)).

$$\Delta P_{bend} = P_r - P_j + \rho_{air} g\left(y_r - y_j\right) \tag{14}$$

For a given geometry, the evolution of ΔP_{bend} can be related to the incoming gas velocity v_r thanks to a polynomial equation, as illustrated in Fig. 24 for three different geometries of the injection pipe. The relation, given by Eq.(15), corresponds to the sum of a singular pressure

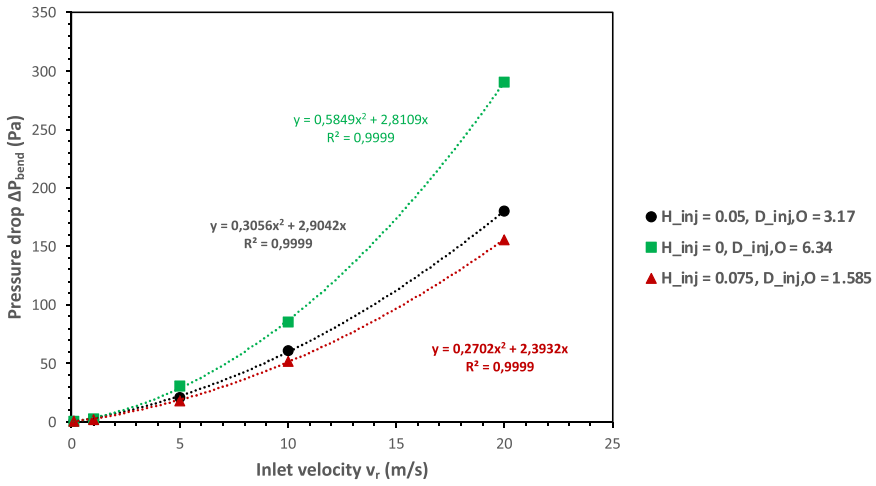

Fig. 24. Evolution of ΔP_{bend} (as deduced from CFD computations) as a function of v_r, for three different geometries of the injection pipe.

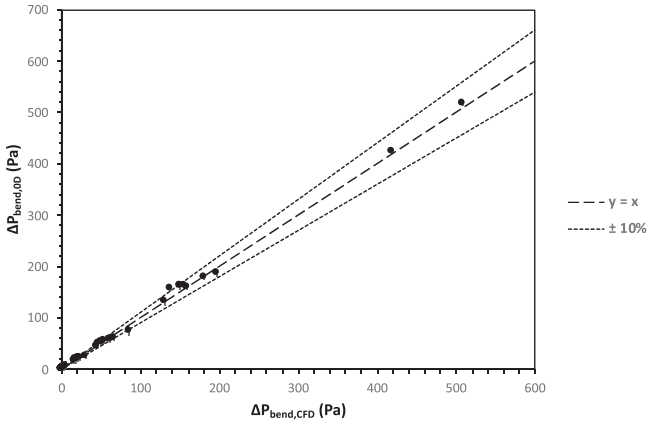

Fig. 25. Assessment of the correlation for ΔP_{bend}: parity plot of the values derived from CFD simulations and those calculated from Eq.(15).

drop, due to the irregularity of the tube section, and a regular pressure drop, due to the friction on the tube walls.

$$\Delta P_{bend} = A v_r^2 + B v_r \tag{15}$$

In Eq.(15), A and B coefficients depend on the outern dimensions of the injection pipe. Correlations for the two coefficients are proposed in Appendix B as function of the geometry.

Finally, Fig. 25 shows the parity plot of ΔP_{bend}. It compares the values calculated by Eq.(15) against the ones derived from CFD simulations using Eq.(14). The dashed lines represent the reference line (perfect agreement) and the ± 10 % deviations. The proposed correlation fits very well the pressure drop due to the injection pipe inside the bend.

4.2.2. ΔP_{aspi} (left side of the loop)

The second pressure variation to be modeled is ΔP_{aspi}, which corresponds to the aspiration induced by the momentum injected into the main reactor. In dedicated simulations, the gas injection is added to the configuration described in Fig. 23, following the same approach as presented in Section 2.2, i.e. using the time and space dependent porosity method. Both the injected mass flowrate $\dot{m}_{inj}$ and the inside diameter of the injection nozzle $D_{inj,I}$ are varied within the same ranges as those considered for the parametric study. Using the macroscopic momentum balance (Eq.(12) and Eq.(13)), ΔP_{aspi} can thus be expressed by Eq.(16). Therefore, its value can be calculated form the CFD simulation results after estimating the pressure drop ΔP_{bend} according to Eq. (15).

$$\Delta P_{aspi} = P_r - P_j + \rho_{air}\left(v_r^2 - v_j^2\right) - \Delta P_{bend} \tag{16}$$

It can be observed that for a given geometry of the injection pipe (i.e. given outern diameter $D_{inj,O}$ and penetration length H_{inj}), $|\Delta P_{aspi}|$ is proportional to the injected momentum, $F_{inj} = \dot{m}_{inj} v_{inj}$ (Fig. 26a). In addition, Fig. 26b represents $|\Delta P_{aspi}|$ as a function of v_r, for fixed values of F_{inj}. It shows that the absolute value of ΔP_{aspi} decreases with the increase of the incoming gas velocity v_r, in a similar way as for regular pressure drops. Indeed, the higher v_r, the further away the mixing of the two gas fluxes is achieved in the pipe (i.e. where the jet vanishes). This means that an increase in v_r increases the distance along which steep velocity gradients exist. Thus, for high v_r, the pressure drop in the mixing zone is high and reduces the aspiration effect.

The linearity of ΔP_{aspi} versus both F_{inj} and v_r allows then expressing the aspiration phenomenon with Eq.(17), where the values of C and D coefficients are given in Appendix B.

$$|\Delta P_{aspi}| = (C v_r + D) F_{inj} \tag{17}$$

Eq.(17) describes the dependence of $|\Delta P_{aspi}|$ on hydrodynamic parameters, but in theory it should also include that of the geometric parameters, i.e. how the C and D coefficients evolve with $D_{inj,I}$, $D_{inj,O}$ and H_{inj}. First, the influence of $D_{inj,I}$ is already taken into account by the F_{inj} term, which depends on this parameter. Second, it is found that ΔP_{aspi} does not vary with the outlet injection diameter $D_{inj,O}$ when the other parameters are fixed (figure not shown). Third, the effect of H_{inj} is likely to be intertwined with that of the other variables for the same reason explained above regarding the steep velocity gradients in the mixing zone. For all these reasons, constant values are kept for C and D coefficients. To assess this hypothesis, Fig. 27 plots the corresponding values of $|\Delta P_{aspi}|$ calculated by Eq.(17) as a function of those obtained from CFD simulations (using Eq.(16)). The different points at about 40 Pa correspond to several values of H_{inj}, whose effect has not been taken into account in the correlation as mentioned above. Nevertheless, the correlation still agrees with the CFD calculations within ± 10 % which validates the proposed approach.

4.2.3. $\Delta P_{jetloop}$ (right side of the loop)

Summing the values of ΔP_{bend} and ΔP_{aspi} given by the correlations defined in Eq.(15) and Eq.(17), respectively, it is now possible to calculate the value for the overall pressure loss $\Delta P_{jetloop}$ in the left side of the loop. However, to evaluate the recirculation rate from Eq.(12), another closure equation is required to express the static pressures, P_r and P_j. The approach consists in expressing also $\Delta P_{jetloop}$ as the sum of the pressure drops experienced by the gas flow in the right side of the loop

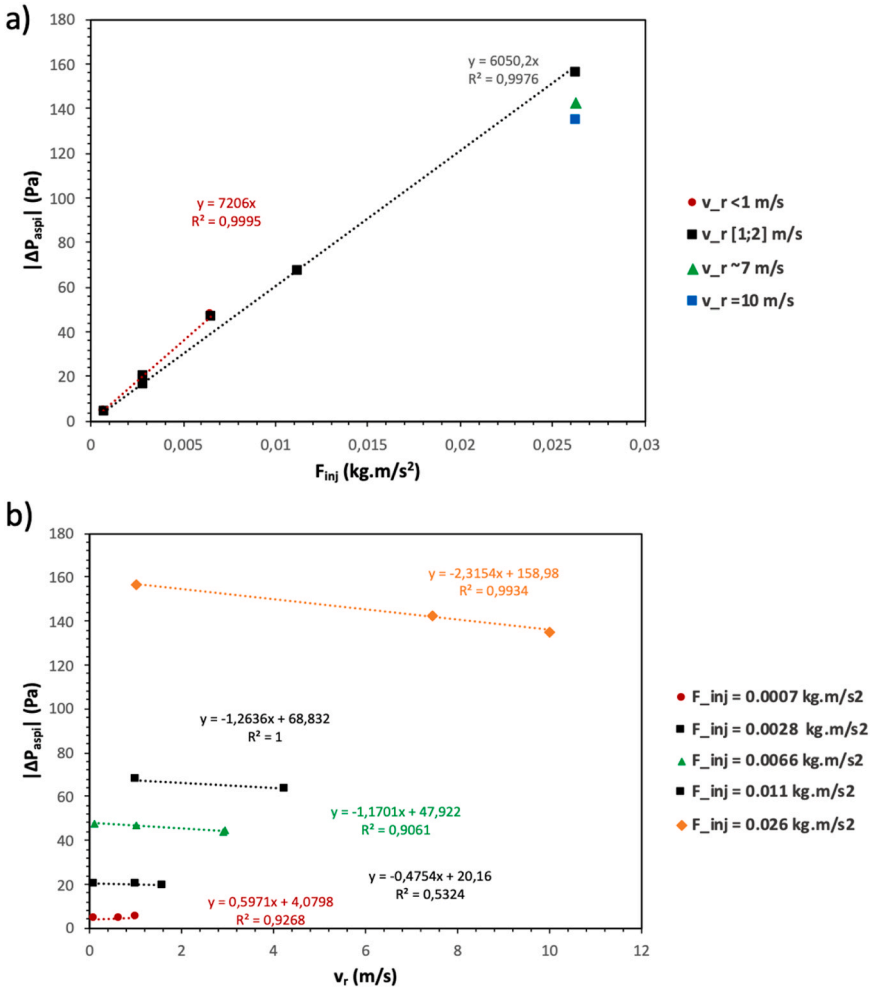

Fig. 26. Evolution of $|\Delta P_{aspi}|$ for a given outern geometry of the injection pipe, a) as a function of F_{inj} for different values of v_r, and b) as a function of v_r for different values of F_{inj}.

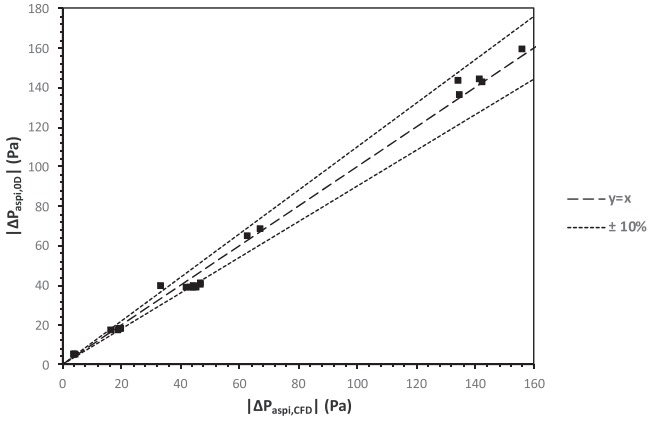

Fig. 27. Assessment of the correlation for ΔP_{aspi}: parity plot of values calculated from CFD simulations and those calculated from Eq.(17).

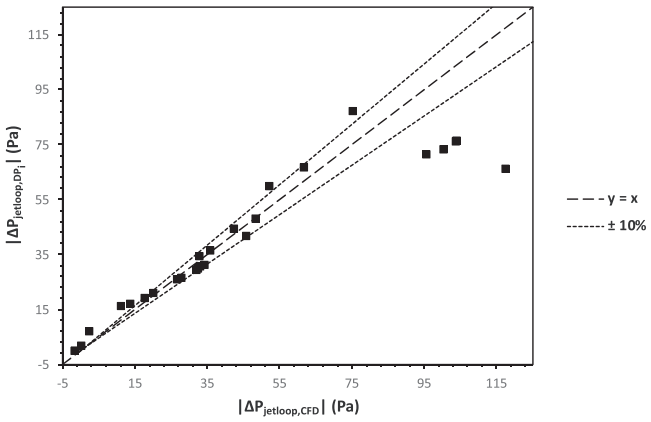

Fig. 28. Assessment of the correlation for $\Delta P_{jetloop}$: parity plot of values calculated from CFD simulations and those calculated as a sum of regular and singular pressure drops in the right side of the loop.

(cf. Fig. 22). Since the effects of the catalyst bed and outlet tube are ignored (see Section 4.1), $\Delta P_{jetloop}$ can then be split into regular and singular pressure drops, respectively due to friction on the pipe walls and to the bends. It is then necessary to differentiate the regions along which the gas flows at the velocity v_j (of length L_j) and the region where the gas velocity is v_r (of length L_r), after the flow division towards the outlet. Assuming that this division occurs just before the bend, the corresponding lengths are $L_j = 1.008$ m and $L_r = 0.691$ m.

Abaci exist to express regular pressure drops as $\Delta P_{reg} = \Lambda \frac{L}{D} \frac{1}{2} \rho v^2$, where L and D are the length and the diameter of the pipe, and the pressure drop coefficient is $\Lambda = \frac{64}{\mathrm{Re}}$ for Reynolds number less than 2300, i.e. laminar flows (Idel'čik, 1986). Singular pressure drops can be

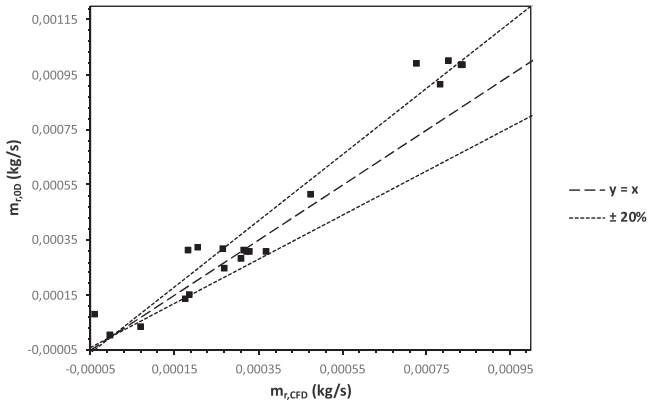

Fig. 29. Validation of the correlation for the recirculation mass flow rate $\dot{m}_r$: parity plot of values calculated from CFD simulations and those calculated from the 0D hydrodynamics model.

classically expressed as $\Delta P_{sing} = K\frac{1}{2}\rho v^2$, where the pressure drop coefficient for a 90° bend in this configuration is $K_{bend} = 0.077$ (Idel'čik, 1986). This is more detailed in Appendix C. Thus, $\Delta P_{jetloop}$ can be finally expressed thanks to Eq.(18). There is also a good agreement between the calculated values and the CFD ones, as demonstrated by the parity plot in Fig. 28.

$$\left|\Delta P_{jetloop,DP_i}\right| = \sum \Delta P_i = \frac{32\mu_{air}}{D_t^2}\left(L_j v_j + L_r v_r\right) + \frac{1}{2}\rho_{air} K_{bend}\left(2v_j^2 + v_r^2\right) \quad (18)$$

The estimated values are lower than the CFD ones for high pressure drops – or high recirculation mass flowrates – in the cases with small injector inside diameters. An explanation lies in the strong jet created in the center of the main tube cross-section in these situations, inducing an inhomogeneity of the velocity field over the tube cross-section. This highlights the limitations of the 0D model, calculated thanks to abaci based on homogeneous cross-sectional velocity assumption.

4.3. Zero-dimensional model confirmation: calculation of $\dot{m}_r$

The initial aim of this 0D hydrodynamic model was to develop a simple relation to calculate the recirculation flowrate $\dot{m}_r$ as a function of the geometric and operating parameters of the jet-loop reactor. The two formulations of the pressure drop $\Delta P_{jetloop}$ obtained from the correlations established in the previous sections can now be equalized (Eqs.(19) and (20)). Finally, developing and regrouping the constant terms, those depending on $\dot{m}_r$ and those depending on $\dot{m}_r{}^2$, the quadratic equation shows in Eq.(21) is obtained, whose coefficients are detailed in Appendix B.

$$\Delta P_{jetloop,0D} = \Delta P_{bend} + \Delta P_{aspi} = \left|\Delta P_{jetloop,DP_i}\right| \quad (19)$$

$$Av_r^2 + Bv_r - (Cv_r + D)F_{inj} + \frac{32\mu_{air}}{D_t^2}\left(L_j v_j + L_r v_r\right) + \frac{1}{2}\rho_{air} K_{bend}\left(2v_j^2 + v_r^2\right) = 0 \quad (20)$$

$$a\dot{m}_r{}^2 + b\dot{m}_r + c = 0 \quad (21)$$

Solving Eq.(21) and keeping the positive root leads to a good agreement with the CFD values, as shown by the parity plot in Fig. 29. With injected mass flow rates $\dot{m}_{inj}$ varying on the same ranges as in the parametric study (i.e. up to 10^{-4} kg/s), the calculated recirculation rates τ_r are up to ~10 (cf Fig. 18 in Section 3.2). In addition, one notes that the correlation slightly overestimates the recirculation rates at high values: this is to be linked to the underestimated pressure loss in the case of velocity inhomogeneity over the loop cross-section.

5. Conclusion

This paper presents a CFD-based design of a jet-loop reactor to be experimentally used for the kinetic study of the catalytic hydrogen oxidation, and more generally to any heterogenous catalytic reaction. The reactor contains a catalyst chamber as a fixed bed – or a short monolith block – of catalyst material, and a high recirculation flowrate is induced to mix the gas phase and minimize the temperature and concentration gradients within the bed. To do so, an injection nozzle penetrates inside the reactor on the opposite side of both the catalyst chamber and the reactor outlet, whose geometric features are optimized.

The *neptune_cfd* code developed for multiphase flow is used, enabling to easily vary the geometric parameters of the reactor thanks to the discrete forcing method (Time and Space Dependent Porosity) and study their influence on the recirculation flowrate, i.e. on the mixing level within the reactor. The key identified parameters are the inside and outside diameters of the injection nozzle and its penetration length, and the inside diameter of the outlet pipe. Effects of operating parameters such as the injection flowrate, the outlet pressure applied, the temperature and the pressure drop created by the fixed bed are also assessed. All these parameters have been varied independently in the simulations to measure the recirculation rate that characterizes the reactor mixing. RTD analyses have also been performed using numerical tracing experiments, so as to calculate the values of the Péclet number for each configuration. Based on these results, an improved design of the jet-loop reactor is proposed, that enables to reach a recirculation rate up to about 9 in the absence of the catalyst bed, and 8.3 taking into account a realistic pressure drop ΔP_{cat} of 50 Pa.

To limit the computational cost of the reactor design, a zero-dimensional hydrodynamic model is developed based on a macroscopic momentum balance, whose specific terms are fitted thanks to dedicated CFD calculations. It allows to understand the establishment of the recirculation, namely due to an aspiration phenomenon of the recycled gas because of the strong momentum injected in the system. Then, a correlation of the pressure drops due to the bend in which there is the injection pipe, which is not listed in the classical abacus, is determined as a function of the incoming gas velocity and its geometric parameters. Furthermore, a correlation is developed to model the aspiration phenomenon, taking into account the effect of the recycled gas velocity and of the injected momentum flowrate. The recirculation flowrates calculated from this 0D approach are in good agreement with those calculated from the CFD simulations, proving the robustness of the model. Both geometric and experimental parameters can thus be varied very easily and quickly to establish a first reactor design and understanding.

The geometric parameters determined by CFD to maximize the mixing level in the jet-loop reactor have been used to manufacture a real reactor. The latter will be used soon to carry out an experimental study of the kinetics for catalytic hydrogen conversion, where the 0D model will help to define the operating conditions depending on the time scale of the reaction rate. The results will be published in a future paper.

Author contributions

R.G.: Conceptualization, Data curation, Investigation, Methodology, Visualization, Writing - original draft. **H.N.** and **W.B.:** Software, Methodology. **R.A.:** Funding acquisition, Resources, Software. **R.A.**, **A-M.B.** and **C.J.:** Project administration, Supervision, Validation, Writing - review & editing.

CRediT authorship contribution statement

Billet Anne-Marie: Writing – review & editing, Validation, Supervision, Project administration. **Julcour Carine:** Writing – review & editing, Validation, Supervision, Project administration. **Neau Hervé:** Software, Methodology. **Benguigui William:** Software, Methodology.

Table 5
Values of the coefficients of Eqs. (16) and (17) for the calculation of ΔP_{bend}.

A_1 (kg/m^4)	A_2 (kg/m^3)	B_1 (kg/m^5.s)	B_2 (kg/m^2.s)
28.1	0.29	13.3 * 10^5	2.14

Table 6
Values of the coefficients in Eq.(19) for the determination of the ΔP_{aspi} correlation.

C (s/m^3)	D (m^{-2})
−97	6144

Gueguen Ronny: Writing – original draft, Visualization, Methodology, Investigation, Data curation, Conceptualization. **Ansart Renaud:** Writing – review & editing, Validation, Supervision, Software, Resources, Project administration, Funding acquisition.

Declaration of Competing Interest

The authors declare that they have no known competing financial interests or personal relationships that could have appeared to influence the work reported in this paper.

Acknowledgments

This study was funded by REACT EU H2 FEDER project ("ConvCatH2"), European Union and Occitanie Region, France. In addition, it was provided with computer and storage resources by GENCI, France at IDRIS thanks to the Grant 2023-A0162B06938 on the supercomputers Jean Zay, Joliot Curie and Adastra, and at TGCC by CALMIP Grant 2023-P1132.

Furthermore, the present work has been realized in the framework of the joint team called ICMF2E (*Institut Commun de Mécanique des Fluides pour l'Energie et l'Environnement*), a collaboration between IMFT and EDF R&D on fluid mechanic applications for energy, environment and processes.

Finally, the authors would like to thank Pr. Patrick Mills (Texas A&M University Kingsville, USA) for the fruitful discussions on the jet-loop reactor concept.

Appendix A. Mesh convergence

Data concerning the mesh convergence, in terms of the momentum ratio (cf Eq.(7)) versus the number of cells in each mesh, presented in Table 3, are plotted in Fig. 30 below. Convergence is easily observable for the third mesh, selected as reference for the work.

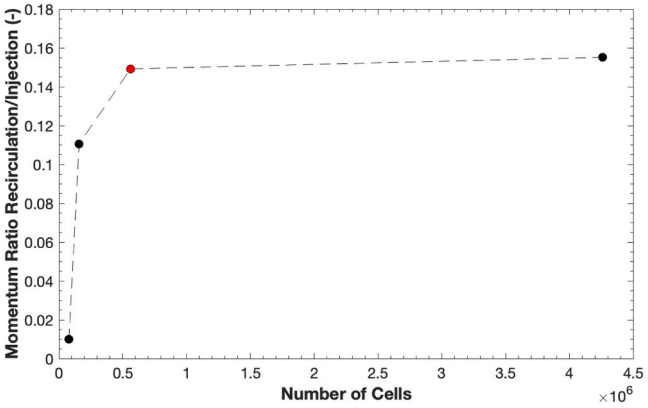

Fig. 30. Impact of the number of cells on the momentum ratio between recirculation and injection

Appendix B. Correlations of the 0D model

Correlations for the A and B coefficients (cf. Eq.(15)) of the 0D hydrodynamic model are developed as follow. First, correlation for the A coefficient proposed in Eq.(22) is derived from the conventional expression of a singular pressure drop: $K\frac{1}{2}\rho v^2$, with K coefficient being expressed by $\left(1-\frac{S_1}{S_2}\right)^2$, and where the sections S_1 and S_2 are respectively the tube section (S_t) and the reduced cross-section $\left(S_t - S_{inj,O}\right)$. Furthermore, the penetration height (H_{inj}) is taken into account adding the constant value $H_0 = 0.021$ m so that the A coefficient is constant when there is no pipe. Regarding the B coefficient, a linear function is derived with both the penetration height and the injector outern section, so that here B is zero when there is no pipe (Eq. (23)). Table 5 gives the values of the different coefficients involved.

$$\mathrm{A} = \mathrm{A}_1 \frac{\left(H_{inj} + H_O\right) S_{Inj,O}^2}{\left(S_t - S_{inj,O}\right)^2} + A_2 \tag{22}$$

$$\mathrm{B} = \mathrm{B}_1 \left(H_{inj} + H_0\right) S_{Inj,O} + B_2 \tag{23}$$

In the same idea, values of C and D coefficients (cf. Eq.(17)) are given in Table 6.

Finally, Eqs.(24) to (26) describe the parameter of the quadratic equation developed for the calculation of the recirculation mass flowrate given in Eqs.(20)-(21).

$$a = \frac{1}{\rho_{air}^2 S_t^2}\left[A + \frac{3}{2}\rho_{air} K_{bend}\right] \tag{24}$$

$$b = \frac{1}{\rho_{air} S_t}\left[B - C\frac{\dot{m_{inj}}^2}{\rho_{air} S_{inj,1}} + \frac{32\mu_{air}}{D_t^2}\left(L_j + L_r\right) + 2K_{bend}\frac{\dot{m_{inj}}}{S_t}\right] \tag{25}$$

$$c = \frac{\dot{m_{inj}}^2}{\rho_{air}}\left[\frac{K_{bend}}{S_t^2} - \frac{D}{S_{inj,1}}\right] + \frac{\dot{m_{inj}}}{\rho_{air} S_t}\frac{32\mu_{air}}{D_t^2} L_j \tag{26}$$

Appendix C. Calculations of regular and singular pressure drops

Known abaci, available in (Idel'čik, 1986), are used to calculate the regular and singular pressure drops involved in the overall pressure drop $\Delta P_{jetloop}$ (cf. Eq.(18)).

First, the regular pressure drop term, ΔP_{reg}, is due to friction of the fluid. It can be calculated as $\Delta P_{reg} = \Lambda \frac{L}{D} \frac{1}{2}\rho v^2$, where L and D are the length and the diameter of the pipe, and the pressure drop coefficient Λ depends on the flow regime. For Reynolds number less than 2300, i.e. laminar flows which is the case in the main reactor loop, $\Lambda = \frac{64}{\mathrm{Re}}$, thus one can express the pressure drop as $\Delta P_{reg} = \frac{32\mu_{air}}{D_t^2} L v$. For Eq.(18), distinction has been made between the regions along which the gas flows at the velocity v_j (of length L_j) and the region where the gas velocity is v_r (of length L_r), after the flow division towards the outlet.

Then, the singular pressure drop term, $\Delta P_{sing} = K_{bend}\frac{1}{2}\rho v^2$, is here due to bends, with the pressure drop coefficient K_{bend} depending on the geometry only. For a bend of angle $\alpha = \pi/2$ radians, of internal diameter $D_t = 1.1$ cm and a curvature radius $R = 3.8$ cm, the pressure drop coefficient is 0.077 (Eq.(27)). Again, a distinction has been made according to the gas velocity: two bends at v_j, and one bend at v_r (cf. Eq.(18)).

$$K_{bend} = \frac{\alpha}{\pi}\left[0.131 + 1.847\left(\frac{D_t}{R}\right)^{7/2}\right] \tag{27}$$

References

Ansart, R., García-Triñanes, P., Boissière, B., Benoit, H., P.K. Seville, J., Simonin, O., 2017. Dense gas-particle suspension upward flow used as heat transfer fluid in solar receiver: PEPT experiments and 3D numerical simulations. Powder Technol. 307, 25–36. https://doi.org/10.1016/j.powtec.2016.11.006.

Baraglia, F., Benguigui, W., Denèfle, R., 2021. A corotational finite element approach coupled to a discrete forcing method to solve hyperelastic deformation induced by two-phase flow. J. Fluids Struct. 107, 103403. https://doi.org/10.1016/j.jfluidstructs.2021.103403.

Battaglia, A., Fox, P., Pohland, F.G., 1993. Calculation of residence time distribution from tracer recycle experiments. Water Res. 27, 337–341. https://doi.org/10.1016/0043-1354(93)90093-W.

Benguigui, W., Archer, A., Pichon, H., 2024. From Reduced- to Full-Scale Validation of a Numerical Model of Air Entry in a Penstock Pipe During Safety Valve Closing. In: Gourbesville, P., Caignaert, G. (Eds.), Advances in Hydroinformatics—SimHydro 2023 Volume 2, Springer Water. Springer Nature Singapore, Singapore, pp. 297–313. https://doi.org/10.1007/978-981-97-4076-5_22.

Benguigui, W., Doradoux, A., Lavieville, J., Mimouni, S., Longatte, E., 2018. A discrete forcing method dedicated to moving bodies in two-phase flow. Numer. Methods Fluids 88, 315–333. https://doi.org/10.1002/fld.4670.

Benguigui, W., Laviéville, J., Merigoux, N., 2019. Fluid-structure interaction in two-phase flow using a discrete forcing method. Numer. Methods Fluids 91, 247–261. https://doi.org/10.1002/fld.4753.

Benguigui, W., Peyrard, C., 2024. CFD numerical approach based on a discrete forcing method for FOWT. Presented at the 19ème journée de l'hydrodynamique, Nantes.

Bernoulli, D., 1738. Danielis Bernoulli … Hydrodynamica, sive de viribus et motibus fluidorum commentarii: opus academicum ab auctore, dum Petropoli ageret, congestum. sumptibus Johannis Reinholdi Dulseckeri; Typis Joh. Deckeri, typographi Basiliensis. https://doi.org/10.3931/E-RARA-3911.

Borman, P.C., Bos, A.N.R., Westerterp, K.R., 1994. A novel reactor for determination of kinetics for solid catalyzed gas reactions. AIChE J. 40, 862–869. https://doi.org/10.1002/aic.690400512.

Carberry, J.J., 1964. Designing laboratory catalytic reactors. Ind. Eng. Chem. 56, 39–46. https://doi.org/10.1021/ie50659a007.

Cui, M., Kulkarni, S.R., Wagner, S., Berger-Karin, C., Nagy, A., Castaño, P., 2022. Hydrodynamic characteristics of an internal recycle berty catalytic reactor in batch/continuous or packed/fluidized bed modes. ACS Eng. Au 2, 103–117. https://doi.org/10.1021/acsengineeringau.1c00026.

Deng, Y., Sabatier, F., Dewil, R., Flamant, G., Le Gal, A., Gueguen, R., Baeyens, J., Li, S., Ansart, R., 2021. Dense upflow fluidized bed (DUFB) solar receivers of high aspect ratio: Different fluidization modes through inserting bubble rupture promoters. Chem. Eng. J. 418, 129376. https://doi.org/10.1016/j.cej.2021.129376.

Ergün, S., 1952. Fluid flow through packes columns. Chem. Eng. Prog. 48, 89–94.

Fuchs, S., Hahn, T., 1993. Construction and application of a jet-stirred loop reactor. Chem. Eng. Process.: Process.Intensif. 32, 225–231. https://doi.org/10.1016/0255-2701(93)80004-Z.

Gamba, I.L., Marquez Damian, S., Estenoz, D.A., Nigro, N., Storti, M.A., Knoeppel, D., 2012. Residence time distribution determination of a continuous stirred tank reactor using computational fluid dynamics and its application on the mathematical modeling of styrene polymerization. Int. J. Chem. React. Eng. 10. https://doi.org/10.1515/1542-6580.3057.

Guelfi, A., Bestion, D., Boucker, M., Boudier, P., Fillion, P., Grandotto, M., Hérard, J.-M., Hervieu, E., Péturaud, P., 2007. NEPTUNE: a new software platform for advanced nuclear thermal hydraulics. Nucl. Sci. Eng. 156, 281–324. https://doi.org/10.13182/NSE05-98.

Hoek, I., Nijhuis, T.A., Stankiewicz, A.I., Moulijn, J.A., 2004. Performance of the monolithic stirrer reactor: applicability in multi-phase processes. Chem. Eng. Sci. 59, 4975–4981. https://doi.org/10.1016/j.ces.2004.07.077.

Hulburt, H.M. (Ed.), 1975. Chemical Reaction Engineering—II, Advances in Chemistry. AMERICAN CHEMICAL SOCIETY, WASHINGTON, D. C. https://doi.org/10.1021/ba-1974-0133.

Idel'čik, I.E., 1986. Memento des pertes de charge: coefficients de pertes de charge singulières et de pertes de charge par frottement. In: Nouv., tirage (Ed.), Collection de la Direction des Études et Recherches d'Électricité de France. Éditions Eyrolles, Paris.

Kim, S.Y., Kim, Y., 2019. Review: Hydrogen Tank Explosion in Gangneung, South Korea. Presented at the 2019 Center for Hydrogen Safety Conference, Sacramento, CA.

Kim, J., Yu, J., Lee, S., Tahmasebi, A., Jeon, C.-H., Lucas, J., 2021. Advances in catalytic hydrogen combustion research: catalysts, mechanism, kinetics, and reactor designs. Int. J. Hydrog. Energy 46, 40073–40104. https://doi.org/10.1016/j.ijhydene.2021.09.236.

Levenspiel, O., 1972. Chemical Reaction Engineering, 2nd ed. Wiley, New York.

Li, Y., Li, X., Shi, J., Zhao, Q., Jin, H., 2024. Modelling and numerical analysis on residence time distribution characteristics in continuous high-pressure hydrothermal reactor. Chem. Eng. Sci. 297, 120310. https://doi.org/10.1016/j.ces.2024.120310.

Melo, P.A., Pinto, J.C., Biscaia, E.C., 2001. Characterization of the residence time distribution in loop reactors. Chem. Eng. Sci. 56, 2703–2713. https://doi.org/10.1016/S0009-2509(00)00517-0.

Nagaraj, A., Mills, P., 2013. Novel Jet-Loop Reactor for Kinetic Measurements of Gas-Solid Heterogeneous Catalyzed Reactions Involving Commercial-Scale Particles. Presented at the AICHe Annual Meeting, San Francisco, CA.

Nasser, M., Megahed, T.F., Ookawara, S., Hassan, H., 2022. A review of water electrolysis–based systems for hydrogen production using hybrid/solar/wind energy systems. Environ. Sci. Pollut. Res 29, 86994–87018. https://doi.org/10.1007/s11356-022-23323-y.

Neau, H., Ansart, R., Baudry, C., Fournier, Y., Mérigoux, N., Koren, C., Laviéville, J., Renon, N., Simonin, O., 2024. HPC challenges and opportunities of industrial-scale reactive fluidized bed simulation using meshes of several billion cells on the route of

Exascale. Powder Technol., 120018 https://doi.org/10.1016/j.powtec.2024.120018.
Neau, H., Pigou, M., Fede, P., Ansart, R., Baudry, C., Mérigoux, N., Laviéville, J., Fournier, Y., Renon, N., Simonin, O., 2020. Massively parallel numerical simulation using up to 36,000 CPU cores of an industrial-scale polydispersed reactive pressurized fluidized bed with a mesh of one billion cells. Powder Technol. 366, 906–924. https://doi.org/10.1016/j.powtec.2020.03.010.
Rastegar, S.O., Gu, T., 2017. Empirical correlations for axial dispersion coefficient and Peclet number in fixed-bed columns. J. Chromatogr. A 1490, 133–137. https://doi.org/10.1016/j.chroma.2017.02.026.
Rongé, É ., Peyrard, C., Venugopal, V., Xiao, Q., Johanning, L., Benoit, M., 2023. Evaluation of second and third-order numerical wave-loading models for floating offshore wind TLPs. Ocean Eng. 288, 116064. https://doi.org/10.1016/j.oceaneng.2023.116064.
Tahir, M., Amin, N.S., 2013. Photocatalytic CO2 reduction and kinetic study over In/TiO2 nanoparticles supported microchannel monolith photoreactor. Appl. Catal. A: Gen. 467, 483–496. https://doi.org/10.1016/j.apcata.2013.07.056.
Trambouze, P., Euzen, J.-P., 2002. Les réacteurs chimiques: de la conception à la mise en œuvre. Nouv. éd. mise à jour. ed. Publications de l'Institut français du pétrole. Éd. Technip, Paris.
Welty, J.R., Rorrer, G.L., Foster, D.G., 2014. Fundamentals of Momentum, Heat, and Mass Transfer, 6th ed. John Wiley & Sons Inc.
Yu, X., Shen, Y., 2024. CFD study of the residence time distribution of shaft-injected hydrogen in a blast furnace. Fuel 372, 132193. https://doi.org/10.1016/j.fuel.2024.132193.